Force Feedback for the Patient Side Manipulator of the daVinci Research Kit

by

Anna Novoseltseva

A Thesis submitted to the Faculty of the

WORCESTER POLYTECHNIC INSTITUTE

in partial fulfillment of the requirements for the

Degree of Master of Science in Biomedical Engineering

Worcester, Massachusetts

May, 2018

Approved by:

Prof. Gregory S. Fischer, Advisor
Worcester Polytechnic Institute

Prof. Karen Troy, Committee Member
Worcester Polytechnic Institute

Prof. Loris Fichera, Committee Member
Worcester Polytechnic Institute

Abstract

Teleoperated robotic surgical systems such as daVinci are widely used for laparoscopic surgeries. The currently available daVinci system does not provide haptic feedback. Prior research has shown that the addition of haptic feedback improves surgeons' performance during minimally invasive surgeries. Other authors have implemented haptic feedback in the daVinci robot by placing sensors on the surgical tools, using visual force estimation, and measuring proximal guide wire forces. However, they have faced issues with biocompatibility, time delay, low accuracy, and repeatability. In this work, two strain gauge force-sensing devices were created for the patient side manipulator of the daVinci surgical robot. These devices were designed to be easily added to the existing system. The device mounted on the cannula measures the X-Y components of the forces applied to the tool, and the device mounted on the sterile adapter measures the Z-component of the force. These devices are used for the real-time force feedback in the daVinci robot. The proposed system has high sensitivity and resolution, matches the required force measurement range, and has high signal-to-noise ratio, which implies high signal quality. However, the absolute errors of the currently built devices are high. This work demonstrates fast 3-DOF force measurements on the daVinci robot without any robot modifications. While the present system has significant systematic errors, these can be mitigated by altering the mechanical design to reduce hysteresis and improve the accuracy of the system.

Acknowledgments

I would like to express my gratitude to everybody in the world.

Dedication

This dissertation is dedicated to everybody in the world.

Contents

List of Tables

List of Figures

Acronyms

PSM Patient Side Manipulator

DOF Degrees of Freedom

PCB Printed Circuit Board

ROS Robot Operating System

SD Standard Deviation

SNR Signal-to-noise Ratio

GF Gauge Factor

ADC Analog to Digital Converter

FFT Fast Fourier transform

RMSE Root Mean Square Error

Chapter 1

Introduction

Teleoperated daVinci surgical system is a robot-assisted surgical system that enhances surgeons performance in minimally invasive surgeries by allowing highly precise translation of surgeon‘s hand movements to the instrument’s movements.

The currently available daVinci surgery system has a laparoscopic camera, providing visual feedback to guide doctors during surgery. However, the system does not have any kinesthetic or cutaneous feedback, known as haptics. [1]

During open surgeries, doctors usually get haptic feedback directly or through the surgical tools. In minimally invasive surgeries interaction with patients via long shafts leads to the loss of some force and tactile sense. In robotic surgery systems, surgeons have to manipulate robots indirectly, which leads to an elimination of any haptic feedback. [2]

It is believed that the addition of haptic feedback in the daVinci surgery robot will help to reduce the amount of surgical errors and intra-operative injuries, which will lead to faster post-surgery recovery time and decreased rate of unsuccessful surgeries. [2–4]

There are many technical challenges to overcome in order to implement the haptic feedback in daVinci robot. One of them is getting accurate force readings from the patient side manipulator (PSM). To address this issue, we are trying to create force-feedback device, that can be easily added to the existing surgery system.

Chapter 2

Background

2.1 Teleoperated Surgical Robots

Recently robots started to be extensively used for surgical procedures. The use of robots allows doctors to perform surgical procedures with high accuracy, repeatability and reliability. Which in turn results in reducing operation time, errors and post-operation injuries. Minimally invasive surgeries are beneficial for accurate procedures with minimal access to operated organs, e.g. neurosurgery, eye surgery, cardiac surgery, intravascular surgeries and etc. Use of robots in minimally invasive procedures improves precision and reliabilty of operations. [5]

There are two types of devices used for surgeries, supporting and augmenting. Supporting devices perform secondary functions to support the surgeon. Some of them used for positioning and stabilization purposes of cameras, endoscopic tools, ultrasound probes and etc. Others to increase device dexterity or autonomy (dexterous and autonomous endoscopes).

Augmenting devices are used to extend surgeon's ability in performing an operation. They can be divided in four categories. Hand-held tools are augmenting instruments that used for hand tremors reduction, for dexterity and navigation capability increase. Another type of augmenting devices are cooperatively-controlled tools, where the surgeon and the robot cooperatively manipulate the surgical device (e.g. ROBODOC system, Steady- Hand robot, LARS, the Neurobot, and the AC-ROBOT system). Teleoperated robots are type of augmenting tools, where surgeon (master) controls the movements of a surgical robot (slave) via a surgeon's console (e.g. the daVinci and the Zeus systems). And autonomous tools, which can perform some tasks (suturing and knot tying) autonomously. [5]

Use of teleoperated robots in surgeries can solve many of the conventional surgery problems in terms of more precise manipulation capability, ergonomics, dexterity, and haptic feedback capability for the surgeon. They enhance dexterity by increase of instrument degrees of freedom, hand tremor compensation, and movements scaling that allows transformation of the control grips large movements into small motions inside the patient. 3-D view with depth perception gives surgeons ability to directly control a stable visual field with increased magnification and maneuverability. All of these enhances the surgeon's operation performance. However, robot-assisted surgeries are high cost, need large operational room space, do not have established efficacy, and need for tableside assistants. For these reasons ability of hospitals to use surgical robots is low, making their use for routine surgeries improbable. [5]

Today, many surgical robotic systems have been commercially developed and approved by the FDA, such as the daVinci surgical system (Intuitive Surgical, Inc., Sunnyvale, CA) , Sensei X robotic catheter system (Hansen Medical Inc., Mountain View, CA), FreeHand v1.2 (FreeHand 2010 Ltd., Cardiff, UK), Invendoscopy E200 system (Invendo Medical GmbH, Germany), Flex robotic system (Medrobotics Corp., Raynham, MA), Senhance (TransEnterix, Morrisville, NC), Auris robotic endoscopy system (ARES; Auris Surgical Robotics, Silicon Valley, CA, USA), The NeoGuide Endoscopy System (NeoGuide Endoscopy System Inc, Los Gatos, CA). [6, 7]

There is also number of NON-FDA-approved platforms that currently under development or going through clinical trials. For example, MiroSurge (RMC, DLR, German Aerospace Center, Oberpfaffenhofen-Weling), The ViaCath system (BIOTRONIK, Berlin, Germany), SPORT surgical system (Titan Medical Inc., Toronto, Ontario), The SurgiBot (TransEnterix, Morrisville, NC), The Versius Robotic System (Cambridge Medical Robotics Ltd., Cambridge, UK), MASTER (Nanyang Technological University and National University Health System), Verb Surgical (Verb Surgical Inc., J & J/Alphabet, Mountain View, CA, USA), Miniature in vivo robot (MIVR) (MIVR, Virtual Incision, CAST, University of Nebraska Medical Center, Omaha, Nebraska, USA), the Einstein surgical robot (Medtronic, Minneapolis, MN). [7]

The daVinci Surgical System is one of the most commonly used robotic surgical systems. In 2015, over 3400 systems were in use around the world. More than 3 million surgeries were performed worldwide using daVinci system [1]. The system has been approved for various types of surgeries such as cardiac, colorectal, thoracic, urological and gynecologic. However, new systems are emerging on the market, providing features that are absent currently in the daVinci System. For example, in 2017 FDA approved Senhance robotic platform that provides actual haptic force feedback, allowing the surgeon to feel forces generated at the instruments end. In addition, the system uses eye-tracking technology to move the camera at the point the surgeon is looking at, while the daVinci uses a footswitch panel to control the camera movement. Another example is Flex Robotic System, which consists of flexible endoscope for laparoendoscopic surgeries. This system is able to define a non-linear path to surgical target by advancing a flexible telescopic inner-outer mechanism with instruments inside it, whereas instruments in the daVinci system can follow only non-flexible straight path. [7]

Effectiveness of daVinci system in comparison to opened surgery and other systems [8]

2.2 Importance of Haptic Feedback

Write about studies with and without haptic feedback.

It has been shown that incorporating force feedback into teleoperated sys- tems can reduce the magnitude of contact forces and therefore the energy consumption, the task completion time and the number of errors. In sev- eral studies [122, 147, 15], addition of force feedback is reported to achieve some or all of the following: reduction of the RMS force by 30

In [106], a scenario is proposed to incorporate force feedback into the Zeus surgical system by integrating a PHANToM haptic input device into the system. In [85], a dextrous slave combined with a modified PHAN- ToM haptic master which is capable of haptic feedback in four DOFs is presented. A slave system which uses a modified Impulse Engine as the haptic master device is described in [30]. In [107], a telesurgery master- slave system that is capable of reflecting forces in three degrees of freedom (DOFs) is discussed. A master-slave system composed of a 6-DOF parallel slave micromanipulator and a 6-DOF parallel haptic master manipulator is described in [150]. Other examples of haptic surgical teleoperation include [93] and [11]. The haptics technology can also be used for surgical training and simulation purposes. For example, a 7-DOF haptic device that can be applied to surgical training is developed in [56]. A 5-DOF haptic mecha- nism that is used as part of a training simulator for urological operations is discussed in [146].

2.3 Current Approaches

1.3 Haptics for Robotic Surgery and Therapy Incorporating haptic sensation to robotic systems for surgery or therapy especially for minimally invasive surgery, which involves limited instrument maneuverability and 2-D camera vision, is a logical next step in the develop- ment of these systems. To do so, in addition to instrumentation of surgical tools, appropriate haptics-enabled user interfaces must be developed.

1.3.1 Haptic user interface technology In the following, examples of the currently available haptic devices are described. For a more complete survey of haptic devices, see [55].

1.3.1.1 PHANToM The PHANToM from Sensable Technologies Inc. (www.sensable.com) is one of the most commonly used haptic devices and comes in a number of models with different features. PHANToM 1.5A provides six DOFs input control. Of the six DOFs of the arm, depending on the model, some or all are force-reflective. In Figure 1.2a, a PHANToM 1.5/6DOF with force feedback capability in all of the six DOFs is shown.

1.3.1.2 Freedom-6S The Freedom-6S shown in Figure 1.2b is a 6-DOF device from MPB Technologies Inc. (www.mpb-technologies.ca) that provides force feedback in all of the six degrees of freedom. The position stage is direct driven while the orientation stage is driven remotely by tendons. The Freedom-6S features static and dynamic balancing in all axes (see [54] for further design details). 1.3.1.3 Laparoscopic Impulse Engine and Surgical Workstation Originally as part of a laparoscopic surgical simulator, the Laparoscopic Impulse Engine was designed by Immersion Corp. (www.immersion.com). The device can track the position of the instrument tip in five DOFs with high resolution and speed while providing force feedback in three DOFs. More recently, Immersion has developed the Laparoscopic Surgical Workstation (Figure 1.2c), which is capable of providing force feedback in five DOFs. An application example is the Virtual Endoscopic Surgery Trainer (VEST) from Select-IT VEST Systems AG (www.select-it.de). The VEST system uses the Laparoscopic Impulse Engine as its force-feedback input interface for simulating laparoscopic surgery interventions.

1.3.1.4 Xitact IHP The Xitact IHPTM from Xitact Medical Simulation (www.xitact.com) is a 4-DOF force feedback manipulator based on a spherical remote-center-of- motion mechanical structure and was originally designed for virtual reality based minimally invasive surgery simulation [42]. It features high output force capability, low friction, zero backlash and a large, singularity-free workspace. A picture of the Xitact IHP is shown in Figure 1.2d.

Placing force sensors on the surgical instrument [9]

They suggest to the measure of pulling and grasp forces at the tip of surgical instrument. For the design of the compliant forceps, the required compliance characteristics are first defined using a simple spring model with one linear and one torsional springs. This model may be directly realized as the compliant forceps. However, for the compact realization of the mechanism, we synthesize the spring model with two torsional springs that has equivalent compliance characteristics to the linear-torsional spring model. Then, each of the synthesized torsional springs is realized physically by means of a flexure hinge. From this design approach, direct measurement of the pulling and grasp forces is possible at the forceps, and measuring sensitivity can be adjusted in the synthesis process. The validity of the design is evaluated by finite element analysis. Further, from the measured values of bending strains of two flexure hinges, a method to compute the decoupled pulling and grasp forces is presented via the theory of screws. Finally, force- sensing performance of the proposed compliant forceps is verified from the experiments of the prototype using some weights and load cells. 10.1109/TRO.2012.2194889

Making new surgical instrument design [10]

Method In this paper a force-feedback enabled surgical robotic system is described in which the developed force-sensing surgical tool is discussed in detail. The developed surgical tool makes use of a proximally located force/torque sensor, which, in contrast to a distally located sensor, requires no miniaturization or sterilizability. Results Experimental results are presented, and indicate high force sensing accuracies with errors ¡0.09 N. Conclusions It is shown that developing a force-sensing surgical tool utilizing a proximally located force/torque sensor is feasible, where a tool outer diameter of 12 mm can be achieved. For future work it is desired to decrease the current tool outer diameter to 10 mm.

Sensorless estimation methods

Vision based solution [11]

They proposed to use vision based solution with supervised learning to estimate the applied force and provide the surgeon with a suitable representation of it. The proposed solution starts with extracting the geometry of motion of the heart's surface by minimizing an energy functional to recover its 3D deformable structure. A deep network, based on a LSTM-RNN architecture, is then used to learn the relationship between the extracted visual-geometric information and the applied force, and to find accurate mapping between the two. Our proposed force estimation solution avoids the drawbacks usually associated with force sensing devices, such as biocompatibility and integration issues. We evaluate our approach on phantom and realistic tissues in which we report an average root-mean square error of 0.02 N.

SLiding pertrubation observer

This paper suggests a bilateral controller applying sliding perturbation observer based force estimation method. In the suggested bilateral controller, the master control uses impedance control and the slave control uses a sliding mode control (SMC). A torque and force sensorless teleoperation system can be implemented using the suggested bilateral control structure through an experimental evaluation. This paper presents a method of estimating the reaction force of the surgical robot instrument without sensors and attempts to use state observer of control algorithm. Sliding mode control with sliding perturbation observer (SMCSPO) is used to drive the instrument, where the sliding perturbation observer (SPO) computes the amount of perturbation defined as the combination of the uncertainties and nonlinear terms where the major uncertainties arise from the reaction force. Based on this idea, this paper proposes a method to estimate the reaction force on the end-effector tip of the surgical robot instruments using only SPO and encoder without any additional sensors. To evaluate the validity of this paper, experiment was performed and the results showed that the estimated force computed from SPO is similar to the actual force.

Measuring the proximal guide wire force [12]

They measure the proximal guide wire force and the force between the surgeon's hand and the handle used on the Phantom, the force feedback closed-loop control can effectively eliminate the loss of mechanical impedance of force feedback information. The accuracy control of force feedback is greatly enhanced in the aspect of security and the operation efficiency.

Write about all disadvantages of previous methods.

Tools - ¿limited lifetime - find citation

Vision -¿ huge time delays, accuracy

Wire force - ¿ repeatability issue

2.4 Force Sensors

Two general principles dominate in force measurement: piezoelectric and strain-gauge sensors. [13]

Piezoelectric sensors consist of two crystal disks with an electrode foil in between. When force is applied, an electric charge, proportional to the applied force, is obtained and can be measured. Piezoelectric sensors show small deformation when force is applied, this results in a high resonance frequency. Also, piezoelectric sensors due to their principle of operation have significant linearity error and drift. [14]

In the strain gauge based force transducers the force causes deformation and subsequent linear change in resistance. Strain gauges are usually connected to a Wheatstone bridge circuit, where the output voltage is proportional to the applied force. Strain gauge based transducers provide small individual errors (200 ppm), show no drift, and are therefore appropriate for long-term monitoring tasks. However, they are relatively big, temperature dependent, and have lower resonance frequency in comparison to piezoelectric sensors. [13, 14]

On the basis of the above mentioned, piezoelectric sensors are preferable for dynamic measurements of small forces while strain gauge sensors are better when large forces are measured. In this study, strain gauges were used since they show better accuracy and long-term stability. [13, 14]

We can use QTC-pills, but it has no-linearity and hysteresis issues. We can test in the future.

2.5 Contributions

Force sensing devices for measuring forces in X-Y direction and one for Z-direction measurement were created. They allow to get accurate force readings from the daVinci tools of the PSM. These devices can be easily added to the existing daVinci system. Since we have to add created device on each robot arm only, it is cheaper than placement of sensors on each separate surgical tool. Moreover, created devices allow to get force data faster than through visual data processing method.

Chapter 3

Methods and Results

3.1 Force Measurement

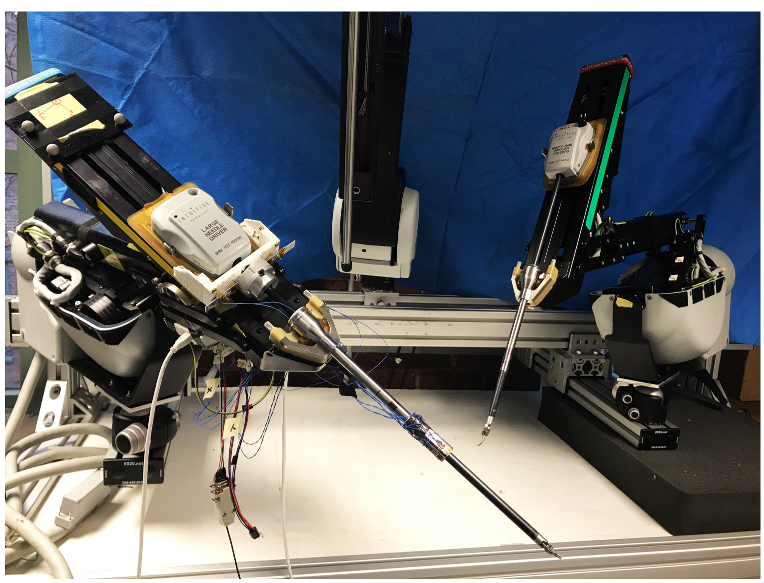

Figure 3.1: Developed Force Measuring System Attached to the PSM

Block diagram of the created system for 3-DOF force measurement is shown on

Figure 3.2. Forces that applied on the end of surgical tool are measured using strain gauges, which change their resistance with force. Using created printed circuit boards (PCBs), this resistance changes are measured and published within ROS. At the same time we measure current joint position of the tool, which is needed for the force calibration. The position data and data from PCBs are used to find values of the force in X,Y,Z directions.

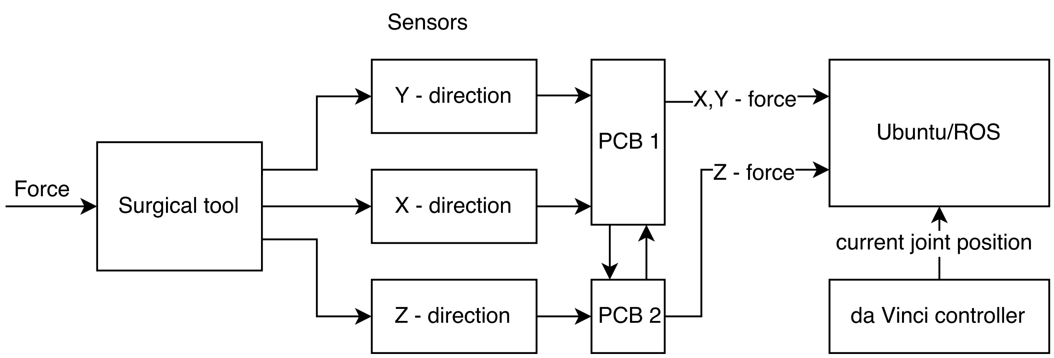

Figure 3.2: Block Diagram

3.2 Sensor Placement Optimization

A finite element analysis was done in Solidworks to assess better placement of the strain gauges on the created device. In order to run finite element analysis material properties, such as elastic modulus, poisson's ratio, and density are necessary to know. Sleeve material is aluminum 6061, that has elastic modulus 68.9 GPa, poisson's ratio 0.33, and density 2700 kg/m^3 [15]. Since the shaft and cannula materials are unknown, in order to run finite element analysis their elasticity modulus and density were found

Table 3.1: Elasticity Modulus Measurement Data

Component	d_o, mm	d_i, mm	I, mm^4	m, g	F, N	L, mm	L_{tot}, mm
Shaft	8.4	6	$1.808 \cdot 10^{-10}$	250	3.25	276.2	366.8
Cannula	10.54	8.75	$3.181 \cdot 10^{-10}$	555	6.011	95.5	105.55

Component	$\delta \pm SD$, mm	$E \pm SD$, GPa
Shaft	2.856 ± 0.123	44.31 ± 1.86
Cannula	0.086 ± 0.004	63.92 ± 2.97

experimentally.

3.2.1 Elastic Modulus Measurements

Elastic Modulus of the shaft and the cannula were found experimentally (Figure 4.2). One end of the observing sample (shaft/cannula) was fixed and the force was applied on the other end. We used weights 250g for the shaft and 555g for the cannula to apply forces. The deformation caused by forces was detected with dial indicator. Experiment was done 5 times, average displacement value was used to calculate elastic modulus. Results are shown in Table 3.1.

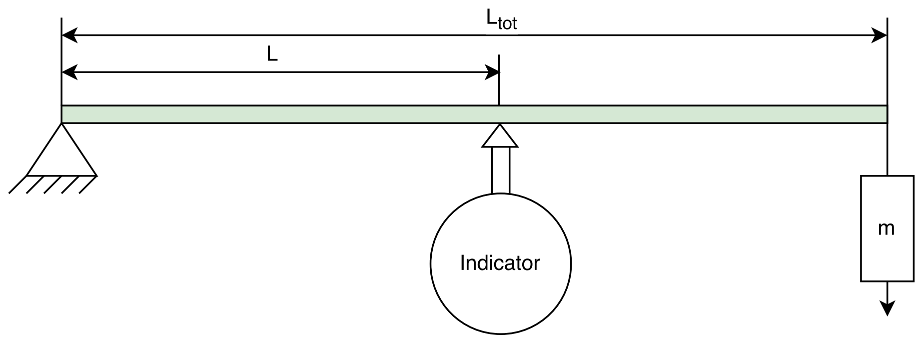

Figure 3.3: Setup to Measure Elastic Modulus

Elastic Modulus was found using following equation:

$$E = \frac{FL^3}{3\delta I} \tag{3.1}$$

where F - force, L - length from the fixed point to indicator, I - area moment of inertia, δ - displacement.

Area moment of Inertia:

$$I = \frac{\pi(d_o^4 - d_i^4)}{64} \tag{3.2}$$

where d_o - cylinder outside diameter, d_i- cylinder inside diameter.

Force acting on indicator:

$$F = \frac{L_{tot}}{L} mg \tag{3.3}$$

where L_{tot} - total length of the object, m - mass of the weight, g - gravitational constant.

Experimentally found mean value of elastic modulus of the shaft is equal to 44.31 GPa with standard deviation (SD) 1.86 GPa, elastic modulus of the cannula is 63.92 GPa with SD 2.97 GPa.

3.2.2 Density Measurements

Density was found using following equation:

$$p = \frac{m}{V} \tag{3.4}$$

where m - mass, V - volume.

Weight was measured using mechanical scale. Volume of the shaft was found by following equation: $V = \pi h(r_o^2 - r_i^2) = 4.36 \cdot 10^{-5} m^3$. Volume of the cannula was found using water displacement method. Shaft material density is 473 kg/m^3, cannula material density is 55238 kg/m^3.

3.2.3 Simulation Results

The mounting location of the active strain gauges should be under the greatest amount of strain. From the Figure 3.4, it can be seen that strain gauges for X-Y direction device should be mounted on the area shown green, that corresponds to strain value approximately equal to $1.5 \cdot 10^{-4}$. Passive strain gauges, that will be used only for temperature compensation, will be placed on the blue area perpendicular to the active strain gauges.

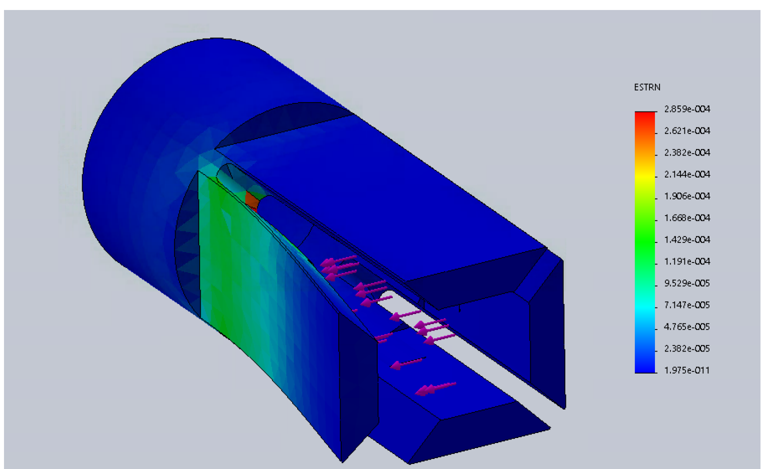

Figure 3.4: Strain in the Device to Measure Forces in X-Y Direction

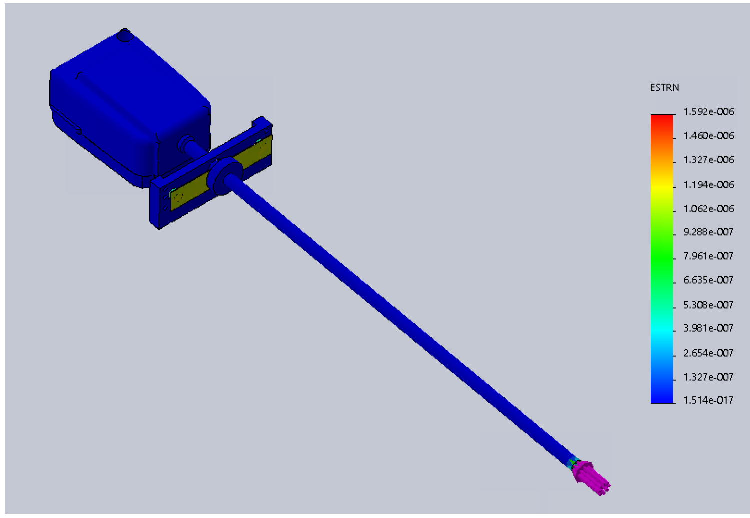

Figure 3.5: Strain in the Device to Measure Forces in Z Direction

Table 3.2: Material Properties

Component	Elastic Modulus, GPa	Density, kg/ m^3
Shaft	44.31	473
Cannula	63.92	55238
Sleeve	68.9	2700

For Z-direction measurement forces (Figure 3.5), area shown with yellow-green color under the highest strain. On both sides and both ends of this plate strain gauges should be placed to form full bridge.

All material properties used for simulations are listed in Table 3.2.

3.3 Requirements for the Device

From the literature review, following requirements for the device were outlined:

Biocompatibility: Z-device is attached to sterile adapter and does not have to be biocompatible. X-Y device goes inside the patient, it means that it should be sterilized and created using biocompatible materials. Current version of the device is not biocompatible. We can achieve biocompatibilty by using Stainless Steel as a device material and biocompatible epoxy to cover strain gauges, also teflon coated wires should be used for all electrical connections.

Force range: Some studies [?, 16, 17] have shown that force range applied during surgeries lies in range (0-11 N). The designed device measures forces in that range, and if the force goes beyond that range it can be used to trigger safety alert.

Force sensitivity: The device should be sensitive enough with minimum detectable signal (MDS) at least 0.3 N and give accurate readings (error ¡ 0.05 N) [16].

Speed of force reading: Device is used for real-time haptic feedback, the minimum requirement for data acquisition speed is 1 kHz [18].

No restriction of motion range of the device: We were able to measure force in three directions independently from each other using separate wheatstone bridges for each direction. At the same time tool can rotate freely and change depth of insertion.

Linearity: Strain gauges have linear response with deformation. Our calibration results have shown linearity of the readings.

Device modularity: Force-sensing devices were designed to fit daVinci cannula and sterile adapter and compensate tolerances by adjustment of set screws.

3.4 Mechanical Design

3.4.1 Strain Gauge

According to the manual for strain gauge selection provided by Vishay Micro-Measurements, the strain gauge should have following parameters:

- Single grid for unidirectional force measurements;
- Isoelastic (D alloy) that has higher gauge factor with E backing;
- Encapsulated with pre attached leads for easier placement;
- STC (self-temperature-compensation) - small temperature dependence;

Maximum strain on the created device is $1.5 \cdot 10^{-4}$, in case of 10 N load with maximally opened shaft. From the literature, strain gauges length should be more than 5% of maximum strain, hence, minimum length of the strain gauge should be 0.0075 mm.

Gauge Factor (GF) for strain gauges usually is 2. According to the formula (3.5) strain gauge with resistance 120 Ω have maximum change in resistance equal to 0.036 Ω, and 350 - 0.105 Ω:

$$\Delta R = GF \cdot R \cdot \varepsilon \tag{3.5}$$

where GF - gauge factor, R - resistance, ε- strain.

For the device strain gauges with resistance 350 Ω, GF is 2, single grid, encapsulated with pre-attached leads were used.

3.4.2 Installation of Strain Gauges

Application of strain gauges was done following the manual provided by Vishay Micro-Measurements. [19].

First the working surface (glass) and tweezers were cleaned with Neutralizer 5. After that shaft surface preparation was started, using solvent degreaser GC-6 Isopropyl Alcohol. A gauge layout was then applied with a 4H drafting pencil. The surface was then conditioned with Conditioner A and the extra liquid was wiped with gauze. Finally, the surface was then neutralized with M-Prep Neutralizer 5A. [19]

The strain gauges were first placed on the glass and then transported using mylar tape onto the instrument surface. A thin layer of catalyst was applied on the strain gauge and given one minute to dry. Then adhesive M-BOND 200 was applied on the surface, pressure was applied on the tape for one minute, then two more minutes to let it dry before the tape was removed. Then leads soldering was done by application of pats, and soldering them with thin wires. [20]

The methodology of the strain gauge application more specifically described in [19].

In compliance with the literature [19] for application of the strain gauge on metals, the same materials and technique can be used. Therefore, the same method was used to apply strain gauges on different materials.

3.4.3 X-Y Device

XY-device consists of one sleeve and one set screw. We manufactured sleeve using Aluminum 6061 Alloy. The manufactured sleeve is placed on the cannula end and is fixed with a set screw on the top.

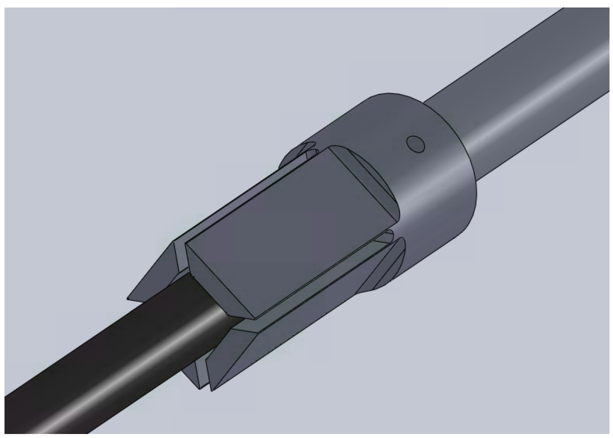

Figure 3.6: XY-direction Force Feedback Sensor

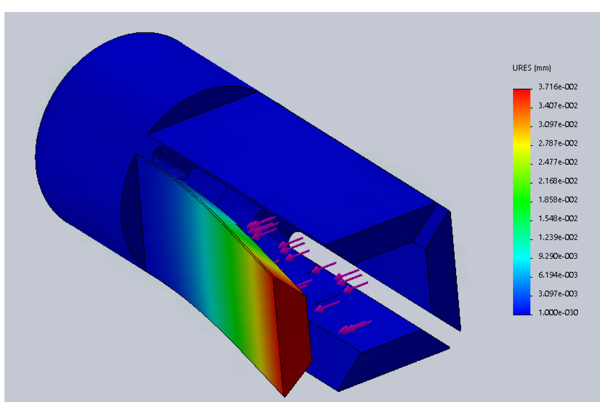

Figure 3.7: Displacement of the XY Device

In order to get accurate readings maximum displacement of the sleeve sides should prevent shaft from hitting the cannula. It means that it should be less than $d = (d_{can_in} - d_{shaft_out})/2 = (8.75 - 8.4)/2 = 0.175$ mm. From the Solidworks simulation (Figure 3.7), maximum displacement is 0.037 mm, which is in appropriate range.

3.4.4 Z Device

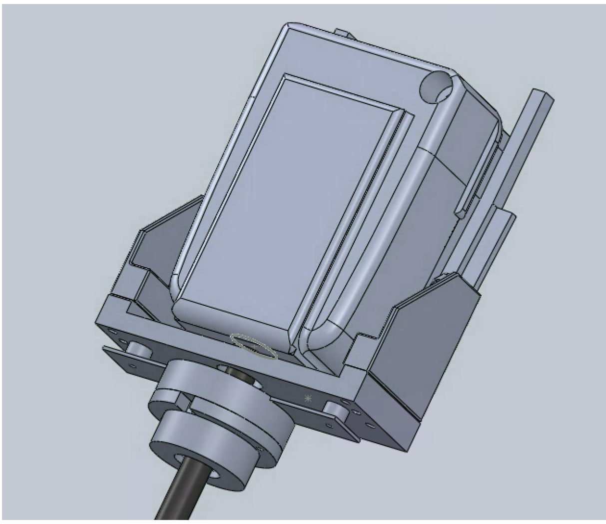

Figure 3.8: Z-direction Force Feedback Sensor

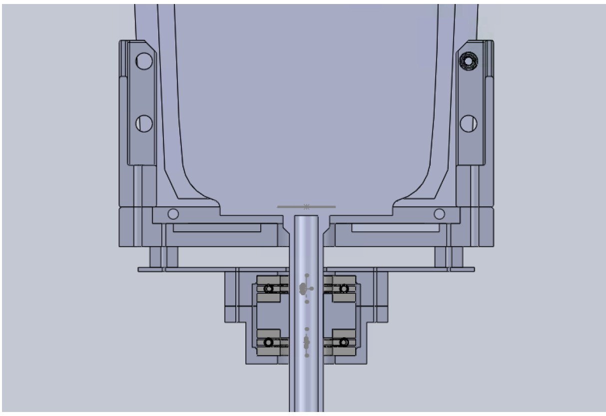

Figure 3.9: Z-direction Force Feedback Sensor (Section View)

Z-device (Figures 3.8, 3.9) consists of attachment to the sterile adapter, 2 thrust ball bearings, three rings, plate, and two cylindrical spacers. Three rings and two ball bearings are used to transfer only z-directional forces further to the plate and keep ability of the shaft to rotate. The ring in the center is in direct contact with the instrument shaft, two outer rings are for the push and pull forces transfer. The plate experience maximum strain and all strain gauge sensors are mounted on it. Two cylindrical spacers are used to give plate space to move and they are mounted on the attachment plate. the attachment plate consist of three plates, they are press fitted on the sterile adapter and fixed with four set screws.

Three rings and plate were manufactured with Aluminum Alloy 6061, attachment parts were 3-D printed, fasteners were used as spacers.

3.5 Electrical and Software Design

3.5.1 Circuit design

Block diagram of the developed PCB is shown on Figure 3.10. Signal waveforms are shown on Figure **??**.

Four strain gauges are connected to form a wheatstone bridge circuit. On Figures 3.11 - 3.12 placement of strain gauges (1-4) and their wheatstone bridge configurations are shown for both devices. Strain gauges deform due to applied forces, and it causes voltage change on wheatstone bridge. Output signal from the wheatstone bridge goes to the instrumentation amplifier. Since ADC can convert only positive voltage,

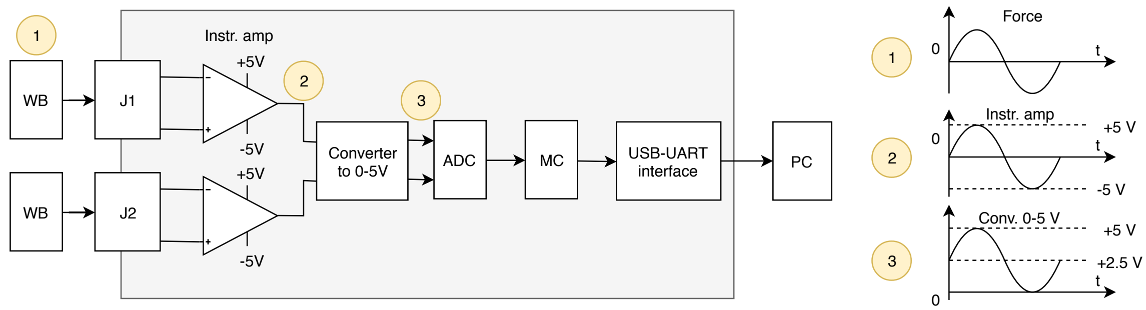

Figure 3.10: Block Diagram of the Circuit

voltage converter changes voltage range of the output signal from $(-5V$ to $+5V)$ to $(0V$ to $+5V)$ range. That signal is converted to digital signal with 16-bit ADC, which communicates with the microcontroller via SPI interface. The output signal is transferred to the computer via USB.

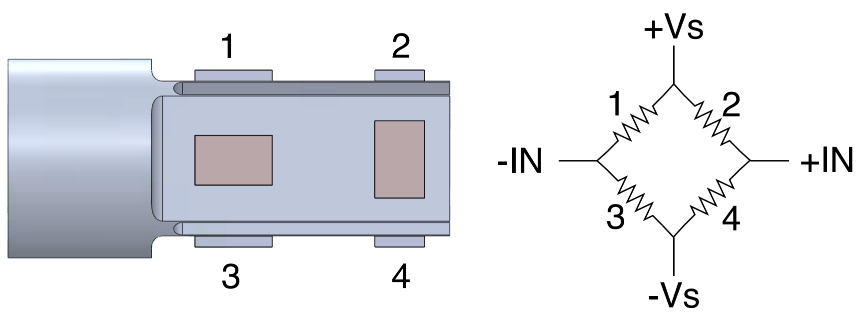

Figure 3.11: Wheatstone Bridge Configuration of the XY-device

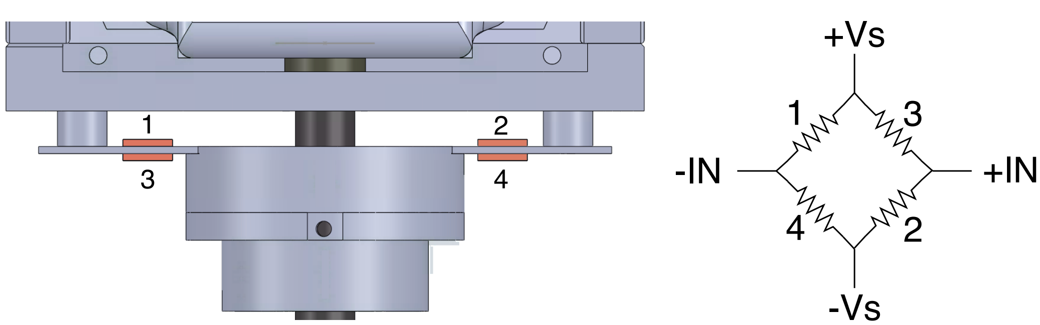

Figure 3.12: Wheatstone Bridge Configuration of the Z-device

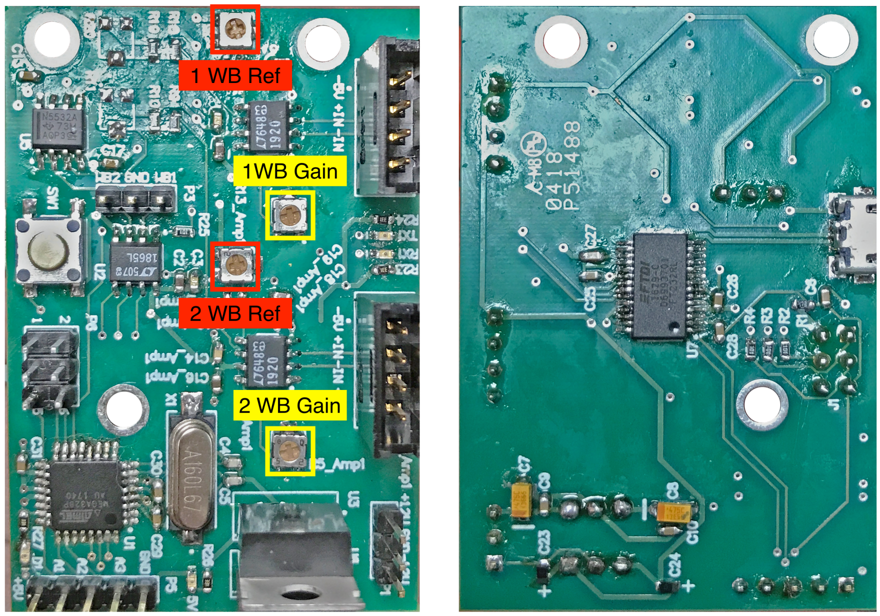

Figure 3.13: Manufactured PCB

Using Altium Designer 15.1 the PCB design was developed and manufactured at Advanced Circuits [21].

In the developed PCB (Figure 3.13) trimpots are used for calibration of the instrumentation amplifier gain (shown yellow) and change of reference voltage (shown red).

Instrumentation amplifier gain change is needed to set up appropriate measuring force range (0-11 N). During calibration, when 11 N applied on the tool end, the output signal (that goes to ADC) should be smaller than 4 V. When the same force applied in the opposite direction, the output signal should be bigger than 1 V.

Reference voltage change is used for the compensation of wheatstone bridge unbalance caused by strain gauge resistance tolerances. During the calibration, it should be tuned until it gives the output signal close to 2.5 V, when no forces applied on the device.

More details on the developed PCB are on github link.

3.5.2 Noise Analysis

Fast Fourier transform (FFT) waveform analysis of the noise signal was performed using Tektronix MSO 4034 Mixed Signal Oscilloscope. The oscilloscope automatically applied the Hanning window, which has good frequency resolution and reduced spectral leakage [22].

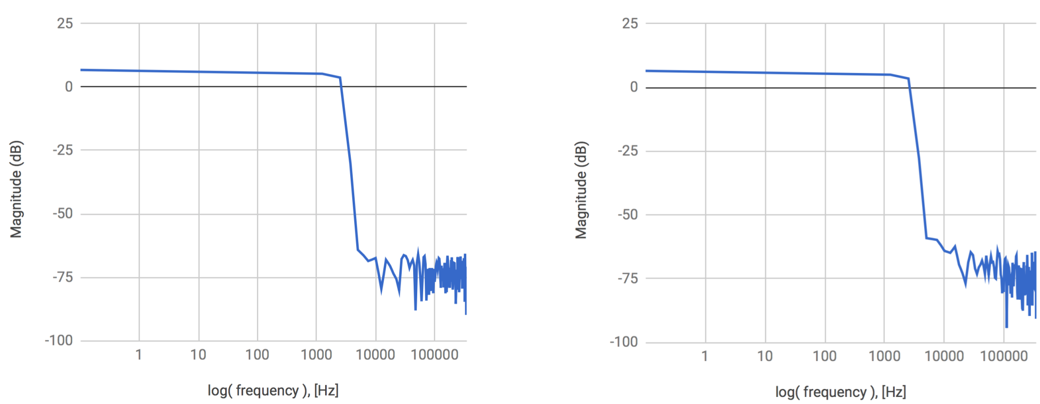

(a) 1st Channel (b) 2nd Channel

Figure 3.14: FFT Analysis Results

The signal frequency from the force sensor should be in range of (0 to 1 kHz). From the FFT analysis it can be concluded, that the noise frequency is in range (2.5 kHz and higher) with amplitude (-50 mV to 70 mV) for both channels. That means, low pass filter with cutoff frequency 2 kHz should be applied on the output signal.

It was decided to use data averaging due to its simplicity of implementation and small time delays. It is an equivalent of low pass filtering that compensates the high frequency noise [23].

3.5.3 Microcontroller Software

Microcontroller ATMEGA328P is used in the developed PCB for acqusition, filtering, and sending data to ROS. Main advantage of this microcontroller is that it has open-source packages for serial communication with ROS. The microcontroller is programmed to initialize ros nodes with names "adc_xy" for XY-device and "adc_zlc" for Z-device. The master-slave communication is created between X-Y and Z- devices for data acquizition synchronization by sending start conversion signals between two PCBs. When one of the devices gets the signal it starts to communicate with ADC though SPI interface (Figure 3.15) [24]. The acquired data is filtered from the high frequency noise by averaging of the 5 most recent readings. And the filtered data is published through the serial port with the baud rate 115200 bits per second.

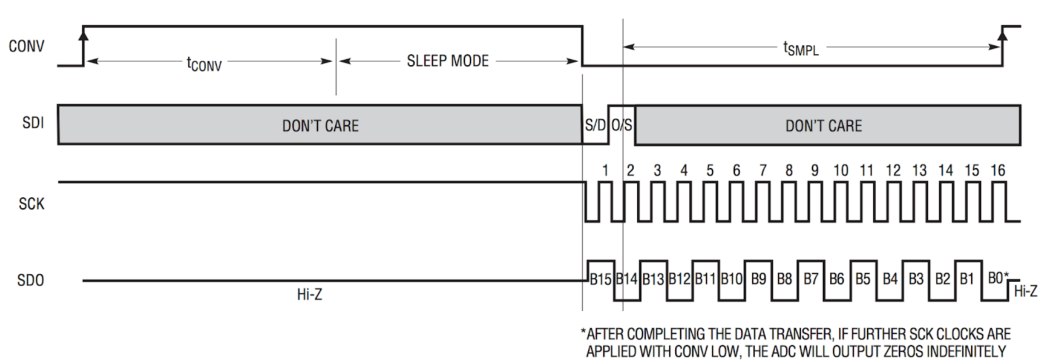

Figure 3.15: LTC1865 Operating Sequence [25]

The github link to master device code and slave-device code.

3.5.4 ROS Architecture

Figure 3.16 shows the ROS architecture of the developed system. In the python script we create a *force_feedback* node. The node is subscribed to X, Y, Z ADC data acquired form sensors and position of the sterile adapter from the daVinci controller. These data are used to find forces. The calculated forces (*force_x, force_y, force_z*) are then published.

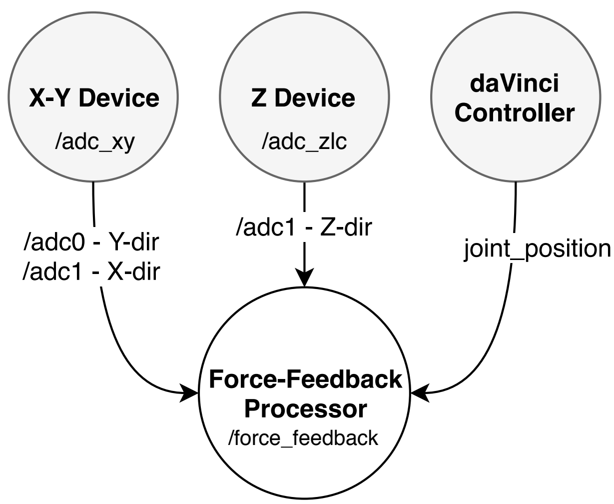

Figure 3.16: ROS Architecture

The program calculates magnitude of the forces in X, Y, Z directions using the calibration equation:

$$F = \frac{adc_{data} - b}{a} \tag{3.6}$$

where b is the constant equal to ADC reading when $F = 0$, adc_{data} is current sensor reading in corresponding direction, and a is linear function of sterile adapter position:

$$a = c \cdot position + d \tag{3.7}$$

where c and d are constants found during calibration and *position* is the position of the sterile adapter.

Z-device readings does not depend on the position of the sterile adapter. Hence, a has a constant value for Z-device.

3.6 Calibration

3.6.1 Calibration Setup

In order to find parameters of the calibration equation (3.6), the calibration system was developed (Figure 3.17). The load cell and Polaris optical tracking system are used to find "true" force applied to the tool end. The load cell is used to find the magnitude of the applied force and the optical markers (4-5) to find the direction of the force.

The calibration of the device starts with calibration of the load cell. The daVinci tool is inserted in the sterile adapter. The force readings depend on the position of the sterile adapter, meaning that the force/sensor readings curve should be found for different positions of the adapter. Finding the curve for only two positions would be enough, because the correlation between the curve and position is linear, as the equation (3.7) shows.

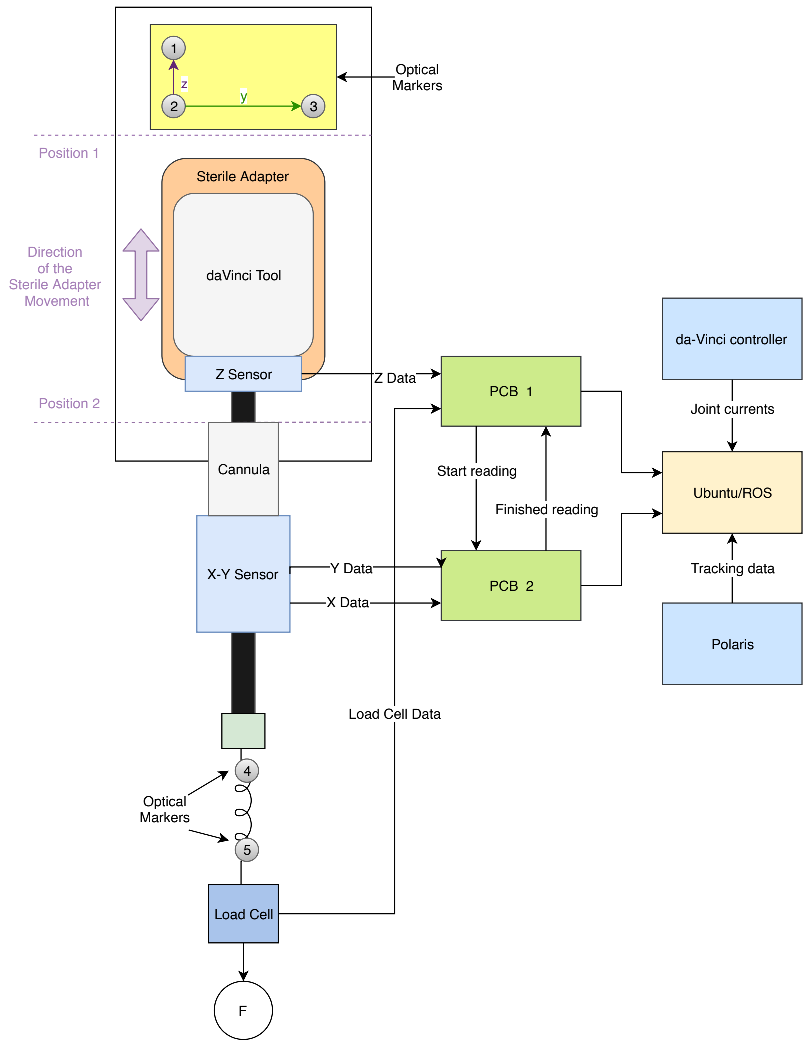

Figure 3.17: Block Diagram of the Calibration Setup

Before starting a data collection, the PSM joint of the sterile adapter is fixed in the position 1. After fixing the adapter, in order to transform Polaris camera frame to the robot frame, the transformation matrix should be found. For this purpose, three optical markers (1-3) are attached to the PSM. Z-direction vector corresponds to the vector formed by optical markers (2-1), Y-direction vector is formed by optical markers (2-3). X-direction vector can be found as a cross product between these two vectors:

$$\vec{X} = \vec{Y} \times \vec{Z} \tag{3.8}$$

The transformation matrix T_c^r is found using coordinates of the $\vec{X}$, $\vec{Y}$, $\vec{Z}$ vectors and coordinates of the optical marker (2) defined as an origin vector.

$$T_c^r = \begin{bmatrix} X_x & Y_x & Z_x & x_0 \\ X_y & Y_y & Z_y & y_0 \\ X_z & Y_z & Z_z & z_0 \\ 0 & 0 & 0 & 1 \end{bmatrix} \tag{3.9}$$

After finding the transformation matrix, the data collection starts. Polaris publishes coordinates of the optical markers (4-5). These coordinates are transformed to the robot frame:

$$P_r = T_c^{r-1} \cdot P_c \tag{3.10}$$

where P_r - coordinates of the marker in the robot frame, P_c - coordinates in the camera frame.

The unit vector of the applied force is found in the robot frame:

$$\vec{U} = \frac{P_5 - P_4}{|P_5 - P_4|} \tag{3.11}$$

where P_5 is the position of the optical marker (5), P_4 is the position of the marker (4), they both are in the robot frame.

The vector of the applied force in the robot frame can be found:

$$\vec{F} = F_m \cdot \vec{U} \tag{3.12}$$

where F_m is the force magnitude found using the load cell. At the same time data from X, Y, Z sensors is collected. The collected data is used to find calibration equation parameters.

3.6.2 Calibration of the Load Cell

The calibration of the load cell is a part of the calibration process of the created device. The bloack diagram of the setup for the load cell calibration is shown on Figure 3.18. The force F was applied on the load cell using weights, its value:

$$F = mg \tag{3.13}$$

where m is mass of the weight and g is the gravitational constant.

The calibration equation for the load cell is following:

$$F_m = adc_{lc} * a_{lc} + b_{lc} \tag{3.14}$$

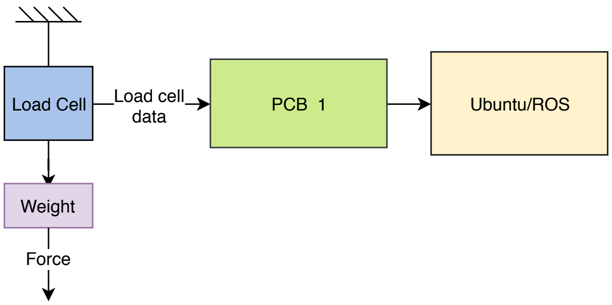

Figure 3.18: Block Diagram of the Load Cell Calibration Setup

where adc_{lc} is acquired ADC data from the load cell; a_{lc} and b_{lc} are constants of the linear equation.

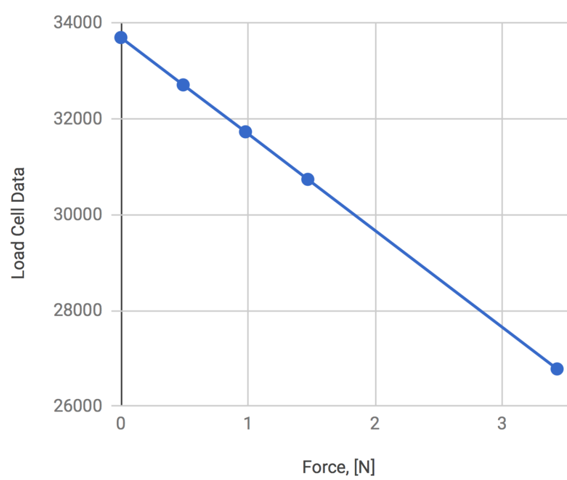

Figure 3.19: Load Cell Calibration Result

Calibration resulted in parameters of the linear equation being $a_{lc} = -4.95 \cdot 10^{-4}$ and $b_{lc} = 16.6$. These values were used to find magnitude of the applied force on the tool end during X-Y and Z devices calibration.

3.7 Results

3.7.1 Calibration Results

The calibration results are shown on Figures **??**, **??**, where blue dots are sensor readings and the calibration function shown as a red line. The results for the Z device are presented on Figure 3.21(a). As an alternative method to evaluate forces exerted in a Z-direction we used joint effort readings (Figure 3.21(b)). This method is simple to implement by subscribing to the joint efforts from the daVinci controller and can be used for performance comparison with created Z-device.

The performance of the created devices was evaluated using standard sensor characteristics, such as absolute error, signal to noise ratio, root mean square error, sensitivity, hysteresis, and measurement range.

All the following infromation about sensor chracteristics is from [26].

The accuracy of the developed sensory systems was assessed using the Root Mean Square Error (RMSE), which is:

$$RMSE = \sqrt{\frac{\sum_{i=1}^{n} \left(\hat{y}_i - y_i\right)^2}{n}} \tag{3.15}$$

where $\hat{y}_i$ is predicted with equation (3.6) force value ; y_i is observed "true" force value found using load cell and Polaris; n is number of observations.

Error is the difference between the actual value of the force and the value produced

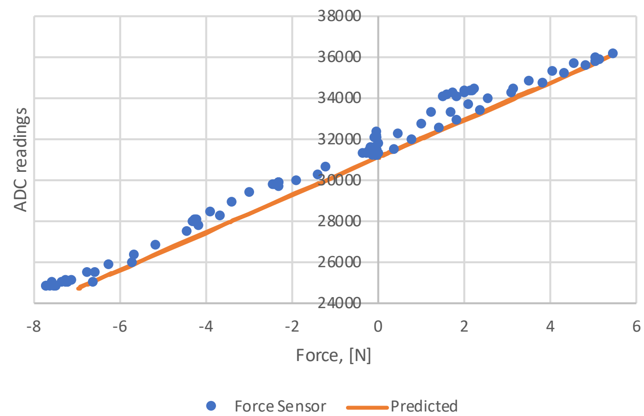

(a) X-direction

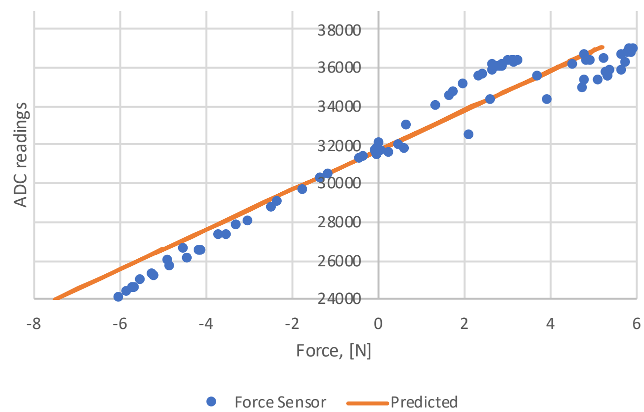

(b) Y-direction

Figure 3.20: Calibration Results of XY Device

by the system (Equation 3.16). Errors are related to accuracy and can be caused by different sources.

$$error = \hat{y}_i - y_i \tag{3.16}$$

One of the measurements of signal quality is signal-to-noise ratio (SNR). A higher value of SNR means the clear acquisitions with low signal distortions and artifacts

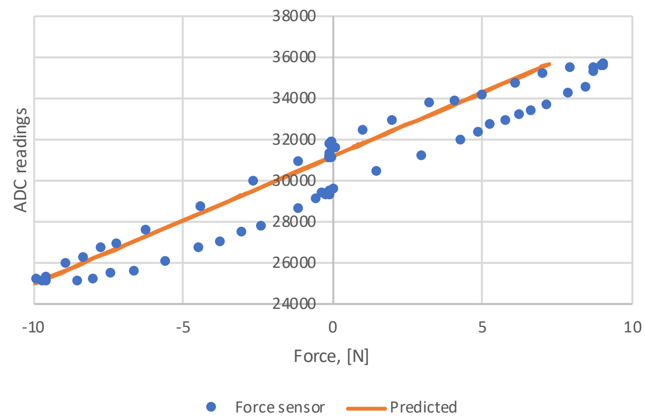

(a) Z Device

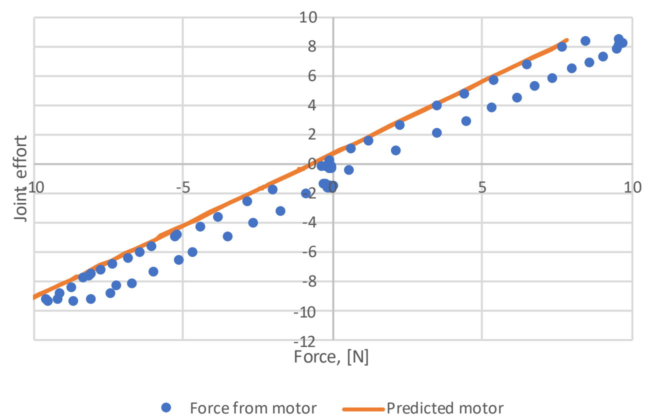

(b) Joint Effort

Figure 3.21: Calibration Results in Z-direction

caused by unwanted noise. It is defined as:

$$SNR = \frac{\mu}{\sigma} \tag{3.17}$$

where μ is mean value of signal, σ is standard deviation of noise.

The slope of the calibration curve is used for the sensitivity S calculation.

$$S = Dy/Dx \tag{3.18}$$

where Dy is the incremental change in the sensors output, Dx is the incremental change of the force.

Resolution is the smallest change of the applied force that gives a noticeable change in the sensor output, it is limited by the signal noise.

Linearity of the system is proximity of the calibration curve to the straight line. R^2 is used to evaluate linearity by measuring closeness of the measured data to the fitted regression line.

Hysteresis is the difference between sensor outputs when the sensor is loaded versus unloaded.

The measurement range consists of the maximum and minimum values of the force that can be measured with created systems. For created system it corresponds to force values, when the output signal reaches saturation. However, for Z-directional measurements, when z-component of the applied force was higher than 12 N it caused sliding of the sterile adapter. Which meaning physical limitation of the system.

Precision represents ability of the system to give the the same output under the same conditions. The precision of the system was assessed by the standard deviation of the sensor outputs, when similar forces were applied.

All sensor characteristics were calculated for X-Y device, Z-device, and Z-direction evaluation joint effort method and provided in the Table 3.3.

Table 3.3: Sensors Characteristics

	X-sensor	Y-sensor	Z-sensor	Joint Effort
Error $\pm$ SD, N	0.059 ± 0.435	0.017 ± 0.755	-0.716 ± 1.324	-1.411 ± 0.672
RMSE	0.44	0.75	1.5	1.56
S/N	2888	3041	114	566
Noise SD, N	0.011	0.004	0.115	0.017
Sensitivity	911	1030	618	0.977
Precision, N	0.4	0.65	0.63	0.35
Resolution, N	0.03	0.02	0.2	0.03
R^2	0.965	0.924	0.938	0.963
Range, N	-19 to 23	-18 to 20	-29 to 34	-12 to 12
Hysteresis, N	0.99	2.4	2.8	1.2

3.7.2 Calibration Curve Dependence from Sterile Adapter Position

Movement of the sterile adapter joint causes change of the moment arm length (L_{gauge} on Figure 3.22).

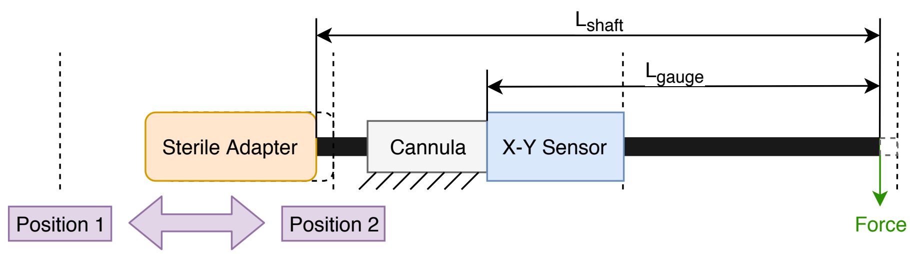

Figure 3.22: Sterile Adapter Movement

The force applied on the X-Y sensor F_{sensor} linearly depends on the moment arm length:

$$F_{sensor} = \frac{L_{shaft}}{L_{gauge}} \cdot F_{tool} \tag{3.19}$$

where F_{tool} is the force applied on the tool end, L_{shaft} is the length of the shaft.

The dependence between position of the sterile adapter and calibration curve constants (a and b from equation 3.6) is linear for X and Y force components (Figures **??**, **??**).

The R^2 of constant a is 0.9 for X-component of the force, 0.827 for Y-component. Low linear fit is caused by considerable systematic errors of the sensors.

Constant b does not depend on the sterile adapter position and changes due to systematic errors and noise in the system.

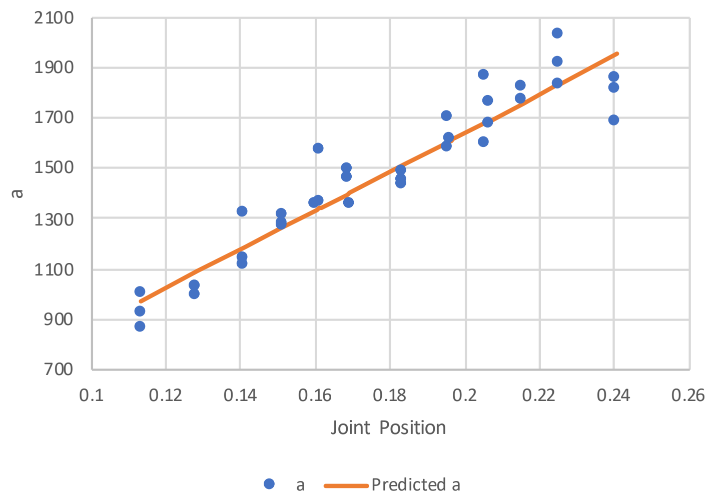

(a) Constant a

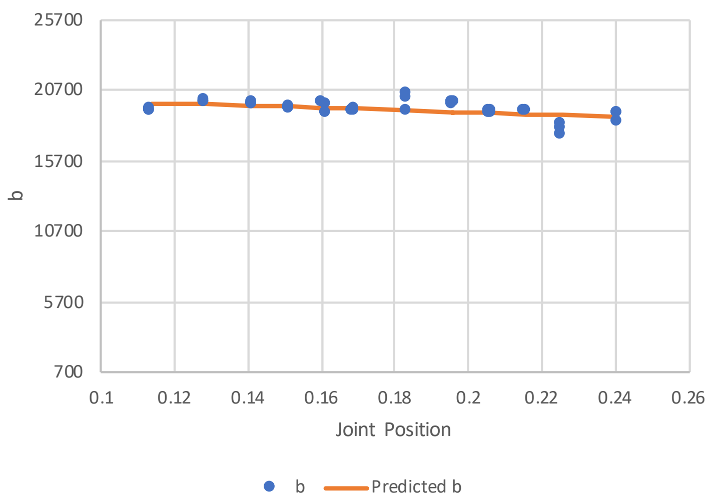

(b) Constant b

Figure 3.23: Sterile Adapter Position Calibration Results for X-direction

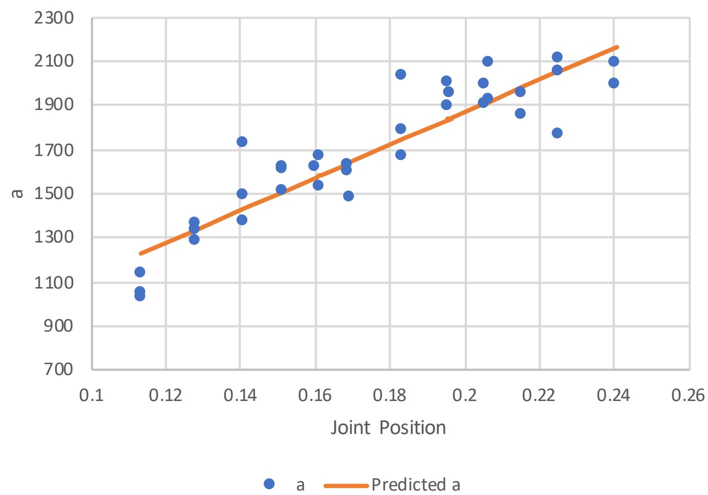

(a) Constant a

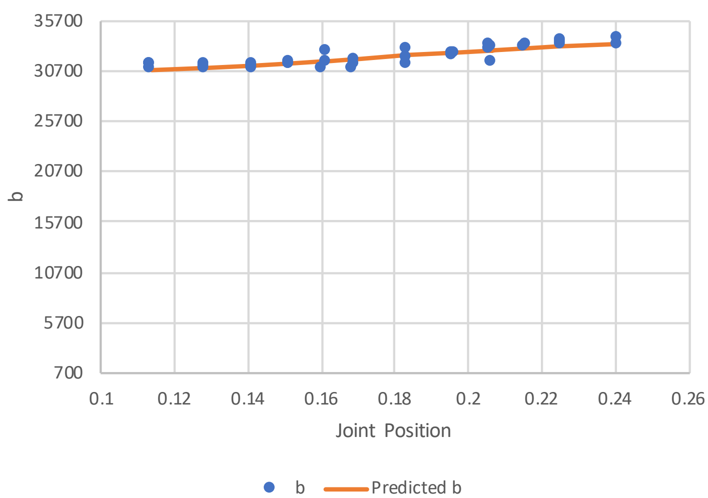

(b) Constant b

Figure 3.24: Sterile Adapter Position Calibration Results for Y-direction

Chapter 4

Discussion and Conclusion

Some of the requirements for the device were satisfied.

Biocompatibility: X-Y device goes inside the patient, it means that it should be sterilized and created using biocompatible materials. Current version of the device is not biocompatible. We can achieve biocompatibilty by using Stainless Steel as a device material and biocompatible epoxy to cover strain gauges, also teflon coated wires should be used for all electrical connections.

Force range: Some studies [**?**, 16, 17] have shown that force range applied during surgeries lies in range (0-11 N). The designed device measures forces in that range, and if the force goes beyond that range it can be used to trigger safety alert.

Force sensitivity: The device should be sensitive enough with minimum detectable signal (MDS) at least 0.3 N and give accurate readings (error ¡ 0.05 N) [16].

The real-time haptic feedback requires minimum data acquisition speed to be 1 kHz [18]. However, the current maximum speed is 588 Hz due to limitation of data transfer using serial communication with computer (115200 bps). In order to increase the speed, we can change the communication channel to one of the wireless protocols, such as SPI (10Mbps), I2C (10k-400 kbps), HDMI (10 Gbps), Ethernet (1 Gbps)

Increase speed form 588 Hz to something higher by change ADC from SPI

communication to parallel communication. Right now maximum frequency is 250ksps, which is 250k/32 = 7.812 KBps.

Change communication channel bw microcontroller and PC to faster one. Right now we use serial port, with max speed 7.1 KBps

Change microcontroller to the faster one.

We can use QTC-pills in future, promising approach, higher sensitivity

No restriction of motion range of the device: We were able to measure force in three directions independently from each other using separate wheatstone bridges for each direction. At the same time tool can rotate freely and change depth of insertion.

Linearity: Strain gauges have linear response with deformation. Our calibration results have shown linearity of the readings.

Device modularity: Force-sensing devices were designed to fit daVinci cannula and sterile adapter and compensate tolerances by adjustment of set screws.

SNR values for all systems are bigger than 1, meaning that all systems have relatively low noise.

Figure 4.1 shows X-component of the force measured with created device and using load cell. SNR of the system is high it can be assumed that fluctuations in the output signal are due to systematic errors.

For Z-direction device we got wide range of forces, because we cannot get high electronic gain, since the sensor is unbalanced caused by mechanical preloading of the sensor plate.

Temperature dependence is not appropriate to do, since we have big systematic errors. First priority will be remove systematic errors.

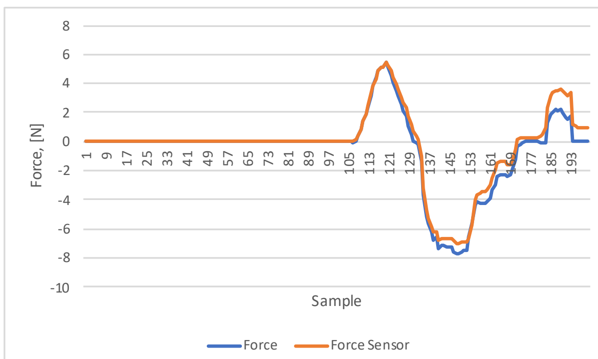

Figure 4.1: Actual and Measured Forces in X-direction

Compare shaft, cannula, sleeve - accuracy, hysteresis.

This is our conclusion)

For future work .. However, disadvantages would be addition of the cost to already expensive system and possible biocompaitibily and sterilization issues. Also addition of the weight to the arm could alter robot performance, however, since the device will be placed close to center of rotation of the robot arm, it will have minimal affect on the moment of inertia in comparison to sensors added to the grippers.

Bio-compatibility and coatings

Sterilization techniques

Since

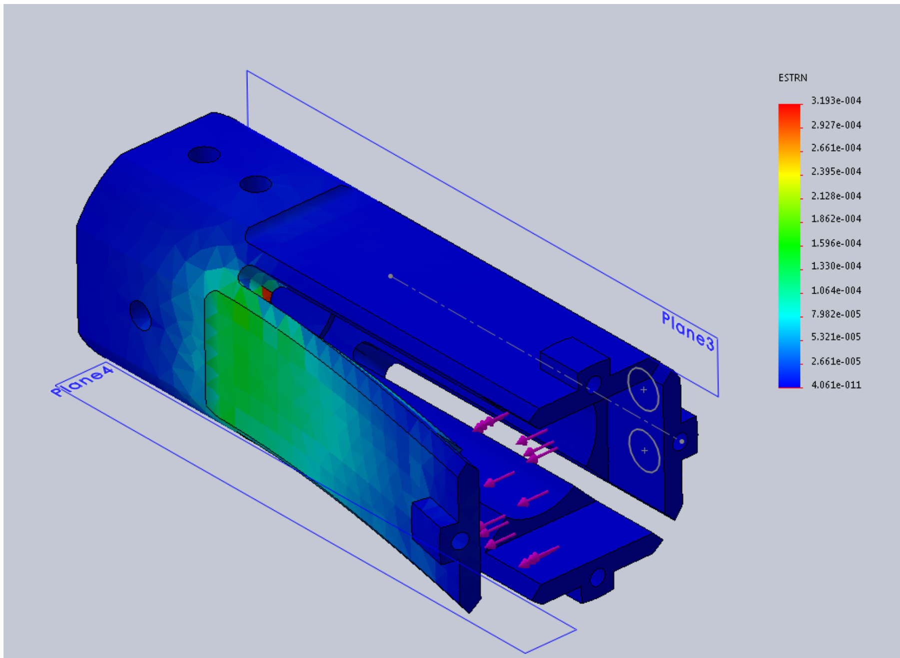

Figure 4.2: Setup to measure elasticity modulus

Z-direction. We tried to measure force in Z-direction, but unfortunately results shown that developed system was not accurate and sensitive enough. To improve system we can suggest to change strain gauges to more sensitive ones. Since we have small room for deformation - around 0.3 mm, we can not afford more deformation by using thinner or longer plates. Therefore, we decided to use motor current readings for z-directional reading of the force.

References

[1] Intuitive surgical, inc. - da vinci surgical system. [Online]. Available: https://www.intuitivesurgical.com/

[2] A. M. Okamura, “Haptic feedback in robot-assisted minimally invasive surgery,” vol. 19, no. 1, pp. 102–107.

[3] C. E. Reiley, T. Akinbiyi, D. Burschka, D. C. Chang, A. M. Okamura, and D. D. Yuh, “Effects of visual force feedback on robot-assisted surgical task performance,” vol. 135, no. 1, pp. 196–202.

[4] O. A. J. van der Meijden and M. P. Schijven, “The value of haptic feedback in conventional and robot-assisted minimal invasive surgery and virtual reality training: a current review,” vol. 23, no. 6, pp. 1180–1190.

[5] M. Tavakoli, *Haptics for Teleoperated Surgical Robotic Systems*. World Scientific, google-Books-ID: 9UNkDQAAQBAJ.

[6] A. R. Lanfranco, A. E. Castellanos, J. P. Desai, and W. C. Meyers, “Robotic surgery,” vol. 239, no. 1, pp. 14–21.

[7] B. S. Peters, P. R. Armijo, C. Krause, S. A. Choudhury, and D. Oleynikov, “Review of emerging surgical robotic technology,” vol. 32, no. 4, pp. 1636–1655.

[8] J. Yu, Y. Wang, Y. Li, X. Li, C. Li, and J. Shen, “The safety and effectiveness of da vinci surgical system compared with open surgery and laparoscopic surgery: a rapid assessment,” vol. 7, no. 2, pp. 121–134.

[9] M. B. Hong and Y. H. Jo, “Design and evaluation of 2-DOF compliant forceps with force-sensing capability for minimally invasive robot surgery,” vol. 28, no. 4, pp. 932–941.

[10] W. Schwalb, B. Shirinzadeh, and J. Smith, "A forcesensing surgical tool with a proximally located force/torque sensor," vol. 13, no. 1.

[11] A. I. Aviles, S. M. Alsaleh, J. K. Hahn, and A. Casals, "Towards retrieving force feedback in robotic-assisted surgery: A supervised neuro-recurrent-vision approach," vol. 10, no. 3, pp. 431–443.

[12] S. M. Yoon, W. J. Kim, and M. C. Lee, "Design of bilateral control for force feedback in surgical robot," vol. 13, no. 4, pp. 916–925.

[13] HBM. (2017) Piezoelectric or Strain Gauge Based Force Transducers? [Online]. Available: https://www.hbm.com/en/3719/piezoelectric-or-strain-gauge-based-force-transducers/

[14] A. sensors. (2017) Piezoelectric Sensors and Strain Gauge-based Force Transducers: Principles in Force Measurement. [Online]. Available: http://www.azosensors.com/article.aspx?ArticleID=281

[15] ASM material data sheet. [Online]. Available: http://asm.matweb.com/search/SpecificMaterial.asp?bassnum=ma6061t6

[16] I. Mack, S. Ferguson, K. Rafferty, S. Potts, and A. Dick, "Interactive force-sensing feedback system for remote robotic laparoscopic surgery," vol. 34, no. 4, pp. 376–387.

[17] S. K. Prasad, M. Kitagawa, G. S. Fischer, J. Zand, M. A. Talamini, R. H. Taylor, and A. M. Okamura, "A modular 2-DOF force-sensing instrument for laparoscopic surgery," in *Medical Image Computing and Computer-Assisted Intervention - MICCAI 2003*, ser. Lecture Notes in Computer Science. Springer, Berlin, Heidelberg, pp. 279–286. [Online]. Available: https://link.springer.com/chapter/10.1007/978-3-540-39899-8_35

[18] Seungmoon Choi and H. Tan, "Effect of update rate on perceived instability of virtual haptic texture," vol. 4. IEEE, pp. 3577–3582. [Online]. Available: http://ieeexplore.ieee.org/document/1389970/

[19] MICRO-MEASUREMENTS. (2014) Surface Preparation for Strain Gage Bonding. [Online]. Available: http://www.vishaypg.com/docs/11129/11129B129.pdf

[20] V. P. Group. Cea Strain Gage Installation with M-Bond 200 Adhesive (Training Video) - Micro-Measurements. Youtube. [Online]. Available: https://www.youtube.com/watch?v=SjXpF61HRys

[21] Printed circuit board manufacturer & PCB assembly | advanced circuits. [Online]. Available: http://www.4pcb.com/

[22] F. J. Harris, "On the use of windows for harmonic analysis with the discrete fourier transform," vol. 66, no. 1, pp. 51–83.

[23] Filtering and smoothing data - MATLAB & simulink. [Online]. Available: https://www.mathworks.com/help/curvefit/smoothing-data.html

[24] Introduction to arduino SPI library with LTC1286 and DAC714. [Online]. Available: https://www.allaboutcircuits.com/projects/arduino-spi-library-ltc1286-dac714/

[25] "LTC1864/LTC1865 - power, 16-bit, 250ksps 1- and 2-channel ADCs in MSOP," p. 24.

[26] K. Kalantar-zadeh, *Sensors Characteristics*. Springer US, pp. 11–28. [Online]. Available: http://link.springer.com/10.1007/978-1-4614-5052-8_2